nature astronomy

Article

https://doi.org/10.1038/s41550-024-02306-8

Evidence of a hydrated mineral enriched in water and ammonium molecules in the Chang'e-5 lunar sample

Received: 4 September 2023

Accepted: 29 May 2024

Check for updates

Shifeng Jin[1,2,8], Munan Hao[1,2,8], Zhongnan Guo[3], Bohao Yin[4], Yuxin Ma[1], Lijun Deng[5], Xu Chen[1], Yanpeng Song[1], Cheng Cao[1,2], Congcong Chai[1,2], Qi Wei[6], Yunqi Ma[6], Jiangang Guo[1,7] & Xiaolong Chen[1,2,7]

The presence and distribution of water on the Moon are fundamental to our understanding of the Earth–Moon system. Despite extensive laboratory research and remote sensing explorations, the origin and chemical form of lunar water have remained elusive. In this study we present the discovery of a hydrated mineral, $(NH_4)MgCl_3{\cdot}6H_2O$, in lunar soil samples returned by the Chang'e-5 mission that contains approximately 41 wt% H_2O. The mineral's structure and composition closely resemble novograblenovite, a terrestrial fumarole mineral formed through the reaction of hot basalt with water-rich volcanic gases, and carnallite, an Earth evaporite mineral. We rule out terrestrial contamination or rocket exhaust as the origin of this hydrate on the basis of its chemical and isotopic compositions and formation conditions. The presence of ammonium indicates a more complex lunar degassing history and highlights its potential as a resource for lunar habitation. Our findings also suggest that water molecules can persist in sunlit areas of the Moon as hydrated salts, providing crucial constraints on the fugacity of water and ammonia vapour in lunar volcanic gases.

The Earth and Moon are often regarded as non-identical twins as they are thought to have originated from a shared giant impact event[1]. On the Earth, water plays a crucial role in planetary evolution through its influence on melting, viscosity, magma crystallization and volcanic eruptions[2,3]. However, initial analyses of lunar samples returned by the Apollo and Luna missions led to the prevailing notion of a dry Moon[4], which imposed important constraints on our understanding of the Moon's formation through a giant impact[5], the existence of a lunar magma ocean[6] and subsequent volcanic activity[7]. In recent years, advances in microanalysis techniques have challenged the concept of a 'dry Moon' through the detection of small amounts of hydroxyl (OH^-) in various lunar samples[8], including pyroclastic glass beads[9], melt inclusions[10], apatite[11] and anorthosite[12]. Estimates of water abundances in the lunar mantle source regions vary widely, ranging from 0.3 to 1,410 ppm (refs. 13,14), with the highest values comparable to those found in mid-ocean-ridge basalt on Earth[10]. Remote sensing and direct impact missions have also confirmed the presence of water molecules (H_2O) in permanently shadowed craters near the lunar poles[15,16]. The large amount of water molecules detected, approximately 5.6% by weight, is commonly believed to be in the form of water ice[17], originating from exogenous sources such as interactions with the solar wind and delivery through impacts[8]. Owing to the low oxygen fugacity (f_{O_2}) on the Moon[18], the release of H_2 vapours is favoured over H_2O vapours during lunar magma degassing[19], and it remains unclear whether

[1]Beijing National Laboratory for Condensed Matter Physics and Institute of Physics, Chinese Academy of Sciences, Beijing, China. [2]School of Physical Sciences, University of Chinese Academy of Sciences, Beijing, China. [3]School of Chemistry and Biological Engineering, University of Science & Technology Beijing, Beijing, China. [4]School of Earth System Science, Tianjin University, Tianjin, China. [5]Center of Advanced Analysis & Gene Sequencing, Zhengzhou University, Zhengzhou, China. [6]Qinghai Institute of Salt Lakes, Chinese Academy of Sciences, Xining, China. [7]Songshan Lake Materials Laboratory, Dongguan, China. [8]These authors contributed equally: Shifeng Jin, Munan Hao. e-mail: chenx29@iphy.ac.cn

https://doi.org/10.1038/s41550-024-02306-8

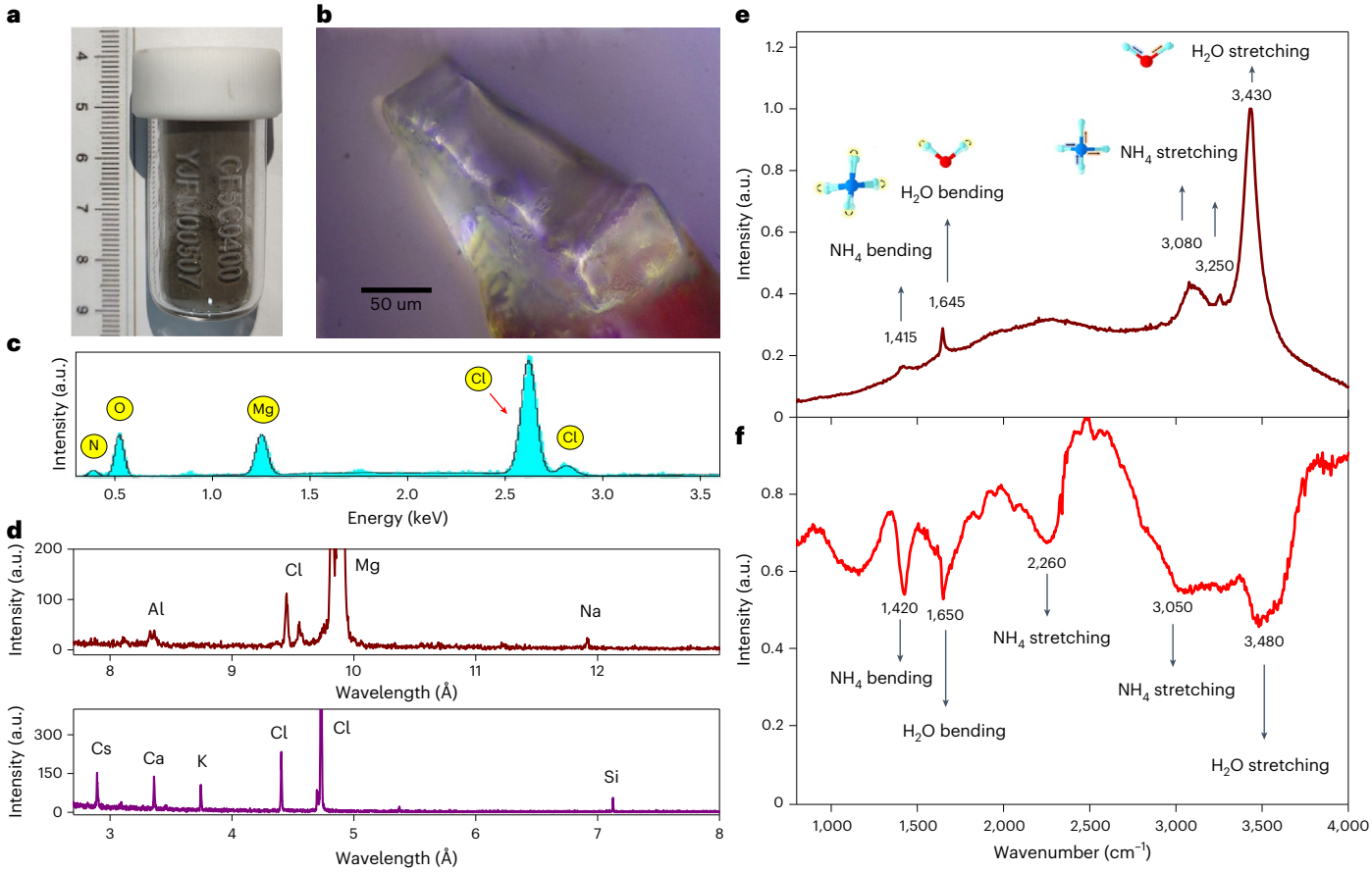

Fig. 1 | Photograph and composition of ULM-1. a, Photograph of the CE5 soil samples. **b**, Photograph of the single crystal of ULM-1 mounted on the top of a cactus thorn. **c**, EDS spectrum. The data (cyan shading) can be fitted (black line) by the presence of N, Mg, O and Cl. **d**, EPMA spectra show the presence of trace elements Cs, Ca, K, Al, Si and Na. **e**, Raman spectrum of ULM-1. **f**, IR spectrum of ULM-1. a.u., arbitrary units.

volcanoes emitting gases have contributed to the lunar hydrosphere[20]. Furthermore, the recent discovery of H_2O on the sunlit regions at high latitudes suggests the existence of lunar water in forms other than water ice, enabling its survival against thermal conditions[21]. The lack of returned lunar samples from high-latitude and polar regions means that neither the origin nor the actual chemical form of lunar hydrogen have been determined. The Chang'e-5 (CE5) mission successfully returned 1.731 kg of lunar soil samples from northern Oceanus Procellarum at 43.058° N (ref. 22); the landing site is at a much higher latitude than the Apollo and Luna missions. The mare basalts from CE5 regolith have been dated at 2.0 Ga using the lead (Pb)–Pb isotope isochron technique[23,24]. Both in situ reflectance spectra and examination of the returned lunar regolith revealed the presence of trace water (OH^-)[25–27], which is mostly attributed to solar wind implantation[25] or hydroxyl-containing apatite[27]. We singled out more than 1,000 mineral clasts (larger than 50 µm) from Sample CE5C0400 (1.5 g, Fig. 1a) with the aid of an optical microscope for Raman measurement, crystallographic study and chemical analyses. Pyroxene, anorthite, olivine, ilmenite and glassy beads make up the majority of the sample, along with a small amount of silica and spinel[28]. A prismatic, plate-like transparent crystal with a size of about 160 × 109 × 73 µm^3 was determined to be an unknown lunar mineral (ULM-1) (Fig. 1b).

The chemical composition of ULM-1 was analysed from fragments of the crystal using both scanning electron microscope (SEM) energy dispersive X-ray spectroscopy (EDS) and electron probe microanalysis (EPMA). As shown in Fig. 1c and Supplementary Fig. 1, the Kα lines of the EDS spectrum suggest that the mineral contains Mg and abundant volatile elements (N, Cl and O, see the measurement details and the choice of standards in the Supplementary Information). The analytical results are presented in Supplementary Table 1, revealing that the ratio of major elements is close to N:Mg:Cl:O = 1:1:3:6. Notably, following repeated measurements of the crystal, there is a rapid decrease in the concentrations of N, Cl and O compared with Mg. Meanwhile, numerous fractures appeared in the petrographic image (Supplementary Fig. 2), suggesting that ULM-1 was undergoing decomposition due to electron beam radiation. More detailed EDS and EPMA measurements revealed the existence of a variety of minor species with concentrations of about 1% or more, including K, Cs, Na, Si, Al, Ca, S, among others, many of which are volatile elements (Supplementary Figs. 3–6). Following examination of different regions of the crystal of ULM-1, it was found that the spatial distribution of these minor elements is highly heterogeneous, even at the micrometre scale (Supplementary Figs. 3 and 4). Fine-scale variations in the composition suggest disequilibrium or rapidly changing equilibrium during its crystallization, or the influence of secondary processes.

The presence of water and ammonium molecules in ULM-1 was confirmed by both the Raman and infrared (IR) spectra (Fig. 1f). The strong normal vibrational modes at 3,430 cm^{-1} (symmetric stretching v_1) and at 1,645 cm^{-1} (bending O–H deformations v_2) of H_2O molecules[29] were clearly observed in the Raman spectrum of ULM-1 as shown in Fig. 1d. Normal modes of the NH^{4+} ion at 3,080 cm^{-1} and 1,415 cm^{-1} were due to its v_1 in phase stretching and v_4 triply degenerate bending, respectively[30]. The band at 3,250 cm^{-1} corresponded to NH_4^+ stretching vibrations[30]. The IR spectrum of ULM-1 clearly shows the major modes of water molecules and NH_4^+ (Fig. 1e). Specifically, the IR absorption at 1,650 cm^{-1} can be attributed to the bending mode of water molecules, which was recently observed in the sunlit moon by the Stratospheric Observatory for Infrared Astronomy remote sensing[21]. Overall, the

https://doi.org/10.1038/s41550-024-02306-8

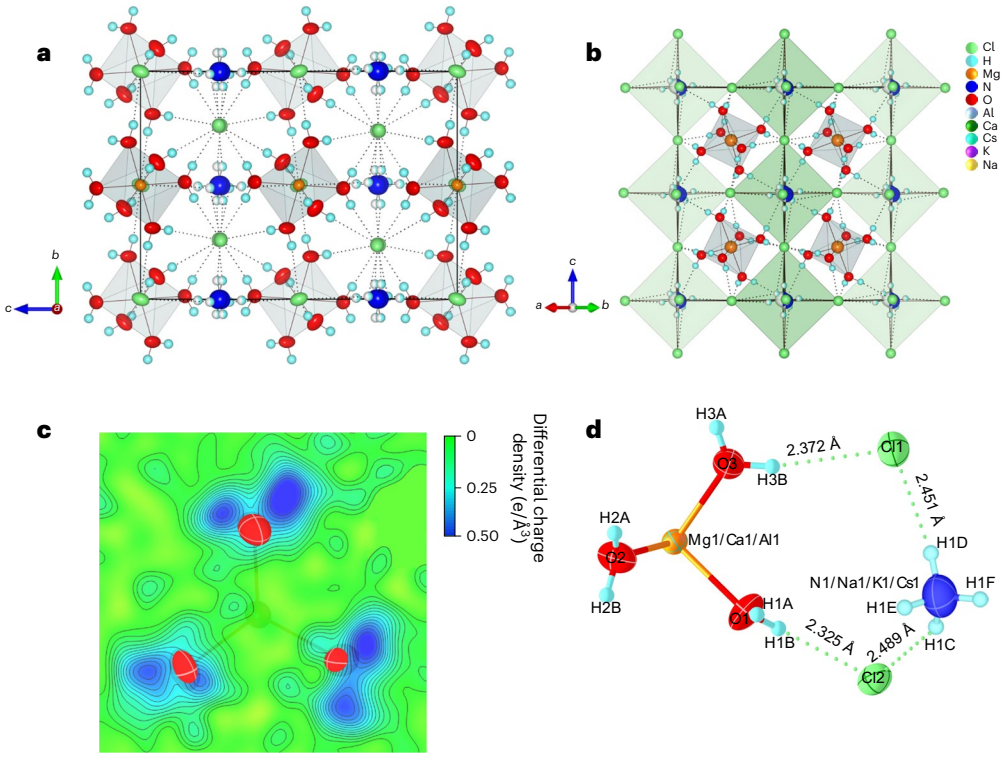

Fig. 2 | Crystal structure and charge density of ULM-1. a, Crystal structure of ULM-1. The dotted lines represent a network of hydrogen bond interactions around the H_2O molecules and NH_4^+ ions. **b**, The mineral crystallized in a perovskite-like structure. The atoms are represented by different coloured spheres according to the element species. **c**, Differential charge density analysis of the regions around all the oxygen atoms shows clear H peaks. **d**, The atoms in an asymmetric unit, in which three independent H_2O molecules in a $[Mg(H_2O)_6]^{2+}$ unit and the NH_4^+ motif are interconnected by Cl^-. The symmetrically distinct atoms have been labelled as different entities. The dotted lines and accompanying values represent the hydrogen bonds and their respective bond lengths.

Raman and IR spectra and the determined chemical compositions of ULM-1 are closely consistent with the observations of novograblenovite $(NH_4,K)MgCl_3{\cdot}6H_2O$ (refs. 31,32), an Earth mineral recently found in basaltic lava from the 2012–2013 Tolbachik fissure eruption at the Plosky Tolbachik volcano[32].

The crystal structure of ULM-1 was determined by X-ray single-crystal diffraction data (Supplementary Table 2). As shown in Fig. 2a,b, the mineral crystallizes in monoclinic space group $C2/c$, with lattice parameters $a = 9.3222(10)$ Å, $b = 9.5731(10)$ Å, $c = 13.3328(12)$ Å, $\beta = 90.101(5)°$ and the number of molecules in a unit cell $Z = 4$. The six independent H atoms on the water molecules are clearly revealed in difference Fourier maps (Fig. 2c). The H atoms in ammonium groups were also revealed and found to be disordered. Subsequent structure refinements revealed nearly full occupancy of the major elements N, Mg, Cl and O, and the trace elements determined by EPMA were complemented to the structure during the last refinements. The final structure parameters and the selected bond lengths and angles are shown in Fig. 2d and Supplementary Tables 2–5, respectively. The chemical formula for ULM-1 is best represented as $[(NH_4)_{0.87}Na_{0.009}K_{0.021}Cs_{0.012}][Mg_{0.97}Ca_{0.023}Al_{0.007}]Cl_3{\cdot}6H_2O$ according to the results of the chemical analysis, structure refinement and the principle of charge neutrality.

In the determined crystal structure, each Mg^{2+} ion is coordinated by six O from water molecules to form a nearly regular octahedron $[Mg(H_2O)_6]^{2+}$; each $(NH_4)^+$ is connected by six Cl^- anions through H–Cl hydrogen bonds to form corner shared octahedra in a 3D framework (Fig. 2b). The crystal structure of ULM-1 is isostructural to novograblenovite[31,32]. It also shares topological similarities with that of carnallite[33], in which nearly all the K^+ cations are replaced by $(NH_4)^+$ molecules. As shown in Fig. 2a, the main units in ULM-1 are interconnected entirely by hydrogen bonds (short dotted lines). Each chlorine atom accommodates six hydrogen bonds: four from O atoms at the vertices of $Mg(H_2O)_6$ octahedra and two from the ammonium ions. The O–H···Cl hydrogen bonds lie in the interval 2.33(2)–2.49(2) Å, while N–H···Cl bonds are normally longer from 2.33(1) to 2.88(1) Å (Supplementary Table 5). Our chemical and structural analyses suggest that ULM-1 is extremely rich in water (41.7 wt%) and ammonia (6.6 wt%). The occurrence of lunar hydrate is surprising, as previous studies have shown that lunar mineralogy is characterized by the absence of water-bearing minerals such as clays, micas and amphiboles[18]. We would like to consider three potential sources for this hydrate, obtained from CE5 lunar soils. First, it may have an intriguing lunar origin as a rare fumarole mineral. Second, it could be a result of contamination from terrestrial sources. Third, it may be a chemical reaction product resulting from the interaction of rocket exhaust with lunar soils during landing. We argue, based on comprehensive chemical, structural and isotopic analysis, that this unusual CE5 hydrate should have a lunar origin.

As is well known, rocks from the Moon and Earth have very similar isotopic ratios for the most abundant elements, but one of the most notable exceptions is lunar chlorine[13,34]. Lunar $\delta^{37}Cl$ values (defined as the per mille variation in $^{37}Cl/^{35}Cl$ relative to standard mean ocean chlorine (SMOC)) have been determined to range from −4‰ to +81‰ (refs. 35,36), far more diverse and higher than observed in any other planetary bodies in the Solar System[13,34–37]. The $\delta^{37}Cl$ values for terrestrial minerals, for instance, only cluster around 0‰ with a typical spread of ±1.0‰ (ref. 34). Exceptionally high $\delta^{37}Cl$ values exceeding +7‰ are only observed in some volcanic gases[34]. In the case of other extraterrestrial minerals, only samples from the Vesta meteorite group and comet coma exhibit $\delta^{37}Cl$ values higher than +9‰ (refs. 38–40) (Fig. 3). The Cl isotope composition of ULM-1 was analysed with a CAMECA 50L nano-scale secondary-ion mass spectrometer (NanoSIMS). To calibrate the matrix effects and instrument mass fractionation, terrestrial $(NH_4)MgCl_3{\cdot}6H_2O$ crystals were synthesized from aqueous

https://doi.org/10.1038/s41550-024-02306-8

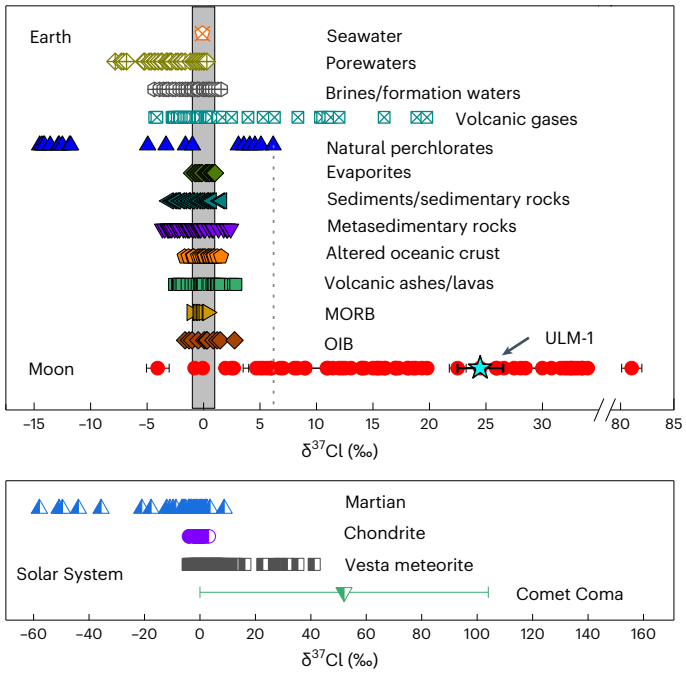

Fig. 3 | Chlorine isotope variability in different terrestrial and extraterrestrial reservoirs. The chlorine isotope composition of ULM-1 is shown as a cyan star, and data are presented as mean values of five measurements ± s.d. The dashed vertical line is the highest value recorded in terrestrial minerals and the grey-shaded band delineates −1.0 to +1.0‰ (all values are relative to SMOC). Almost all evaporite and mid-ocean-ridge basalt (MORB) values fall within this grey band, illustrating that the largest Cl terrestrial reservoirs are near 0‰. A break in the *x* axis is implemented to include the highest value observed on the Moon. The terrestrial and extraterrestrial data are from refs. 13,34–40 and therein. Error bars are 1 s.d.; the error bar of Comet Coma is extraordinarily large (±100%, with n = 7,401); other error bars are either not available or smaller than the symbols. OIB, ocean island basalt.

solution, employing the chemical reagents NH_4Cl and $MgCl_2{\cdot}6H_2O$ purchased from Sinopharm Co., Ltd. The Cl isotopic ratios in the synthetic $(NH_4)MgCl_3{\cdot}6H_2O$ standard were determined using a high-accuracy solid thermal ionization mass spectrometer[41], and the $\delta^{37}Cl$ value was determined to be +0.08(1)‰. Relative to such a small $\delta^{37}Cl$ value in the terrestrial sample, the measured $\delta^{37}Cl$ value of ULM-1 is exceptionally high, up to +24.5‰ on average (see Fig. 3 and Supplementary Table 6 for measurement details). As shown in Fig. 3, the extremely high $\delta^{37}Cl$ value in ULM-1 is much higher than the minerals from terrestrial environments[34]; this $\delta^{37}Cl$ value instead falls well within the range of lunar minerals[35,36].

The determined structure of ULM-1 is isostructural to a terrestrial mineral novograblenovite $(K,NH_4)MgCl_3{\cdot}6H_2O$ (refs. 31,32) and closely resembles carnallite[33], which also shed light on the origin of this hydrate. On Earth, novograblenovite is a rare fumarole mineral that was discovered in Tolbachik volcano only recently. In-depth analysis suggests that this mineral should be formed by a reaction of basalt with hot volcanic gases enriched in H_2O, HCl and NH_3 (ref. 31). Novograblenovite was also found as a sublimate around vents of hot gases in a few burning coal dumps, where the crystallization temperature is slightly above 100 °C (ref. 32). It should be noted that the latter samples without a basaltic origin are free from K and have a simpler formula $(NH_4)MgCl_3{\cdot}6H_2O$ (ref. 32). Compared with the known terrestrial mineral, ULM-1 exhibits a very complicated chemical composition, $[(NH_4)_{0.87}Na_{0.009}K_{0.021}Cs_{0.012}][Mg_{0.97}Ca_{0.023}Al_{0.007}]Cl_3{\cdot}6H_2O$. Sulfur (S) and phosphorus (P) were also detected at certain locations of the ULM-1 crystal (Supplementary Fig. 3). The heterogeneous distribution of calcium (Ca), aluminium (Al), silicon (Si), S, P and various alkali metals in the ULM-1 crystal aligns with the characteristics of a natural mineral formed from a rock–vapour reaction. Furthermore, isotopic fractionation occurring during the degassing of a hydrous melt would result in elevated $\delta^{37}Cl$ in the vapour phase[34]. This phenomenon, observed in HCl-bearing terrestrial volcanic gases, aligns with both the presence of H_2O and HCl vapour necessary for the formation of ULM-1 and the observed high $\delta^{37}Cl$ value. The unique isotope and chemical composition of ULM-1 compared with terrestrial samples strongly suggests that the possibility of laboratory contamination is unlikely.

The oxyhydration of lunar soil in an air atmosphere is well known as the compound FeOOH, arising from the water vapour contamination of indigenous $FeCl_2$, was found in the form of 'rust' in lunar rocks from the Apollo mission[42]. However, the possibility of air contact leading to the formation of the water-rich ULM-1 crystal is highly unlikely. The formation of ULM-1 can essentially be described by the following chemical equations:

$$6H_2O(g) + NH_3(g) + HCl(g) + MgCl_2(s) = (NH_4)MgCl_3{\cdot}6H_2O(s), \quad (1)$$

or

$$6H_2O(l) + NH_4Cl(s) + MgCl_2(s) = (NH_4)MgCl_3{\cdot}6H_2O(s). \quad (2)$$

In either case, the formation of ULM-1 would require abundant ammonia species (NH_3 or NH_4Cl), which are absent in air. The high temperature above 100 °C required for a vapour-phase reaction (equation (1)) or the aqueous environment (equation (2)) required for the crystallization of ULM-1 further help to rule out air contact as the source[31,32].

The formation conditions of ULM-1 in hot vapour phases raise the possibility of rocket exhaust as the source. However, several factors make the rocket exhaust scenario highly unlikely. First, in situ spectral analyses conducted by the CE5 lander on the lunar surface reveal hydroxyl contents within the lower range of the lunar hydration features predicted by remote sensing[25], with no noticeable influence from rocket exhaust. The highest water content observed at the landing site was also found in a CE5 rock with a potential basaltic origin, rather than the lunar regolith, which would be more susceptible to rocket exhaust[25]. Second, the formation of the ULM-1 crystal on the lunar surface requires a reaction between hot, magnesium-rich basalt and eruptive gas exhalations enriched in HCl and NH_3. However, HCl and NH_3 are extremely scarce in rocket exhaust plumes, regardless of the type of fuel used in the main rocket or the lander of CE5 (such as liquid H_2/O_2 and unsymmetrical dimethylhydrazine/N_2O_4). Lastly, the exceptionally high $\delta^{37}Cl$ value of ULM-1 cannot be explained by contamination from terrestrial-sourced rocket exhaust.

Having shown that ULM-1 could have an indigenous lunar origin, it is important to analyse the stability of this hydrate crystal under the harsh lunar environment around the CE5 landing site. It is generally accepted that in permanently shadowed craters, at sufficiently low temperatures, molecular water could be preserved in the form of ice. However, on the sunlit moon, where the lunar conditions have become too harsh for ice to survive, the actual chemical form of lunar water (H_2O) is still unknown. CE5 landed at a relatively high latitude (43.058°), where the lunar surface bolometric temperature does not exceed 80 °C according to the Diviner dataset[43]. Moreover, the thermal conductivity of lunar regolith is very low, meaning that solar radiation only heats up the topmost grains of a few millimetres in thickness (Supplementary Fig. 7). Direct on-site measurements of lunar surface temperature indicate a 50 °C drop compared with Diviner bolometric temperatures[44]. For the shaded surface regolith surveyed by CE5, the highest temperature is expected to be below 30 °C, decreasing to approximately −70 °C for deeper drilled regolith[44]. Compared with water ice, the decomposition temperature of novograblenovite is

https://doi.org/10.1038/s41550-024-02306-8

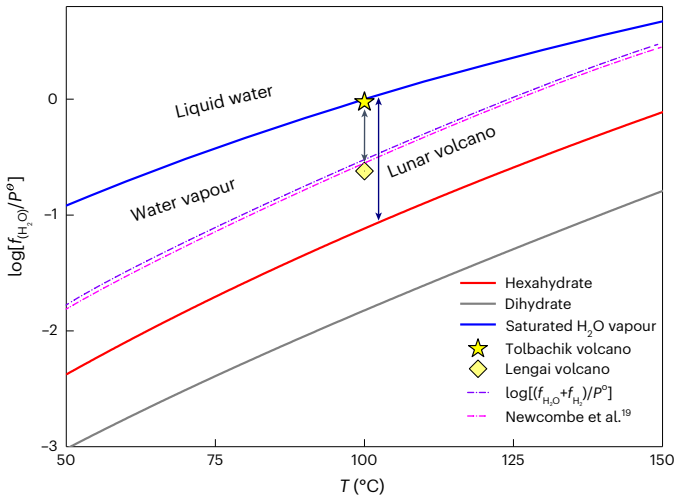

Fig. 4 | Constraints on water fugacity from the crystallization of ULM-1. The hexahydrate is stable above its thermodynamic equilibrium line (red), which constitutes the lower limit of f_{H_2O} for lunar volcanic gases. The vapour–liquid phase boundary of water forms the upper limits (blue). Between the red and grey lines, a dihydrate phase of NLM-1 becomes thermodynamically more stable. Based on the reported formation temperature of the Earth mineral (>100 °C), the lower limit of f_{H_2O} reached one-third of the record value in the driest volcano on Earth: Lengai volcano. When considering H_2 degassing, the $f_{H_2O+O_2}$ values become comparable to that of Lengai volcano[46] based on the H_2/H_2O ratio estimated by Newcombe et al.[19] and our thermodynamic calculations. T, temperature; P^o, standard pressure (1 atm).

reported to be ~90–150 °C higher[32,45], and is stable in a vacuum below 80 °C (Supplementary Fig. 8). The increased thermally stability of this hydrate would be crucial to protect the lunar water (H_2O) from the harsh lunar environment for billions of years. The existence of lunar hydrated salt offers a natural explanation for the water molecule signal recently detected on the sunlit moon[21], as well as the enhanced water (OH^- or H_2O) signals in some pyroclastic deposits[46].

Although the returned lunar basalt is generally highly depleted of water[18], the formation condition of this lunar hexahydrate suggests that during eruption some lunar fumaroles exsolved considerable amounts of water and hydrogen vapour, along with other H-bearing species including NH_3 and HCl. We performed thermodynamic calculations of equilibrium constants in a temperature range from 50 °C to 150 °C (detailed in the Methods and Supplementary Information), allowing us to constrain the fugacity of gaseous water f_{H_2O} in lunar volcanic fumes. On Earth, novograblenovite was found to crystallize from vapours at temperatures slightly higher than 100 °C (ref. 32). We note that the maximum sum of the fugacities of NH_3 and HCl is further thermodynamically constrained by the chemical reaction:

$$NH_3(g) + HCl(g) = NH_4Cl(s) \quad (3)$$

Thus the temperature-dependent lower limit of f_{H_2O} to form ULM-1 can be obtained and delineated by the red curve in Fig. 4. Below this equilibrium line, the hexahydrate becomes unstable and gives way to a known dihydrate: $(NH_4)MgCl_3{\cdot}2H_2O$ (ref. 45). The upper limit of f_{H_2O} is set by the equilibrium between the liquid water and its saturated vapour (blue line). In this temperature range, the lower limit of f_{H_2O} of lunar volcanic gas is constrained to be ~3.5–16.6% of the saturated water vapour. With reference to the formation temperature of terrestrial novograblenovite (>100 °C)[32], the f_{H_2O} of the volcanic gas should be greater than 7.7% of the atmospheric pressure (atm). As a comparison, this lower limit is around three times lower than the f_{H_2O} of the driest Earth volcano—Ol Doinyo Lengai volcano (>24% atm)[47]. It is worth noting that in the Tolbachik volcano, where the Earth mineral is found, the measured f_{H_2O} is higher than 92% atm (pentagon)[3], one log unit higher than the thermodynamic equilibrium value. Moreover, when taking H_2 degassing into account[19,48], the estimated $f_{H_2O+O_2}$ values (purple dotted line) become comparable to Lengai volcano on Earth (as detailed in the Supplementary Information). Considering the potentially distinct volatile contents of pyroclastic eruptions and mare basalts, our results depict a specific phase of lunar volcanic eruption during the crystallization of ULM-1.

The existence of lunar volcanic gases rich in H_2O and H_2 vapours also has implications for the origin of the volatile species detected in permanently shadowed craters. Remote sensing missions have shown that, in addition to H_2O, there are large amounts of solid H_2 and NH_3 in the lunar polar regions[16,49], which are within the lunar volcanic gas inventory revealed here. It is conceivable that some of these volatiles, including water (H_2O), could have originated from magmatic degassing during the eruption of ancient lunar volcanoes. After more than half a century of lunar sampling missions and laboratory research, the presence of molecular water (H_2O) in lunar soil is found, in the form of a well-crystallized hydrate. The structure and composition of this hydrate closely resemble that of the rare terrestrial fumarole mineral novograblenovite, suggesting that the lunar mineral $[(NH_4)_{0.87}Na_{0.009}K_{0.021}Cs_{0.012}][Mg_{0.97}Ca_{0.023}Al_{0.007}]Cl_3{\cdot}6H_2O$ could have formed through reactions involving basaltic lava and lunar volcanic gases rich in H_2O, HCl and NH_3. The low formation temperature of this mineral can also be achieved through diurnal heating or impact gardening on the Moon. While lunar water has typically been attributed to sources such as the solar wind, comets and meteorites, the remarkably high $\delta^{37}Cl$ value of this hydrate suggests that it is more likely to be indigenous to the Moon. The enhanced thermal stability of this hexahydrate compared with water ice, coupled with its high-latitude location, may contribute to the preservation of molecular water on the sunlit moon. This hydrate provides critical constraints on the lowest f_{H_2O} of lunar volcanic gases during its crystallization, with the resulting $f_{H_2O+H_2}$ falling within the range observed in some of the driest volcanoes on Earth.

Methods

EDS

Unlike known lunar mineral samples, ULM-1 evaporated quickly under the electron beams during EDS and especially EPMA. The concentrations of the main elements of ULM-1 were acquired using a Phenom pro XL microscope equipped with an electron microprobe analyser for the elemental analysis in EDS mode (15 kV acceleration voltage; 5 nA beam current). The data acquisition rate was ~10^3 counts per second, with 20–25% dead time and 200 s live time. Element concentrations were measured using the Kα lines for N, O, K, Mg and Cl. X-ray intensities were converted to weight per cent by the XPP quantitative analysis software (Oxford Instruments plc, version 2009)[50]. The standards employed for quantitative analysis were bischofite ($MgCl_2{\cdot}6H_2O$, for elements Mg, O and Cl) and sal-ammoniac (NH_4Cl, for Cl and N). The concentrations of the trace elements of ULM-1 were acquired using a Hitachi S4800 microscope equipped with an electron microprobe analyser EMAX operating in EDS mode (15 kV acceleration voltage; 10 nA beam current). The data acquisition rate was ~10^3 counts per second, with 20–25% dead time and 1,200 s live time. Concentrations of elements exceeding 0.1 wt% can be analysed using this method. The results of the EDS data are presented in Supplementary Figs. 1–3 and Supplementary Table 1.

EPMA

The composition of ULM-1 was analysed using a Shimadzu 8050G electron probe microanalyser. The ULM-1 sample prepared for EPMA analysis was 40 × 50 × 20 μm^3 in size, and the material was carbon coated and prepared as flat sections before insertion into the vacuum. While the spectrum weight of O, N and Cl volatiles decreased substantially relative to Mg under strong EPMA beams, the concentrations of

more stable minor elements (K, Cs, Na, Ca, Al and Si) were acquired with low detection limits down to 100 ppm. An acceleration voltage of 15 kV and beam current of 50 nA were used for all analyses, with a spot size of 10 μm and integration time of 600 s. Data were processed with the ZAF matrix correction using EPMA-Browser software (version 2020)[51]. Forsterite was used as the standard for Mg. The standards used for the other elements analysed were sodium chloride (Cl), silicon dioxide (O), boron nitride (N), potassium feldspar (K), sodium feldspar (Na), pollucite (Cs), elemental aluminium (A)), elemental silicon (Si) and calcium fluoride (Ca). The results of the analysis for ULM-1 are listed in Supplementary Table 1.

Raman measurements

Raman scattering experiments were performed in a quasi-backscattering geometry with the excitation line $\lambda = 532$ nm of a solid-state laser (power $P = 2$ mW). The laser beam was focused to a 3-μm-diameter spot on the surface of the ULM-1 crystal. The spectra were recorded using a WITec α-300R and JY Horiba HR800 spectrometer.

IR spectroscopy

The IR spectrum of ULM-1 was obtained using a SpectrumOne Fourier transform IR spectrometer coupled with an AutoImage microscope with a spectral resolution of 1 or 2 cm^{-1}. The sample was placed on a gold mirror, and the spectrum obtained was a superposition of the transmission and reflectance signals, with strong predominance of the former. Rectangular apertures matching the crystal dimensions (that is 50 × 50 μm^2) were employed.

X-ray crystallography

X-ray diffraction intensities of reflections were collected for the ULM-1 crystal on a Bruker D8 Venture single-crystal diffractometer equipped with a micro-focus X-ray tube (multilayer mirror monochromatized Mo Kα radiation) at room temperature. Data collection, cell refinement and data reduction were carried out in the Bruker APEX4 program (version 2021). All calculations were performed with SHELX programs in the framework of an Olex2 software package (version 1.3)[52]. ULM-1 crystallizes in the monoclinic space group $C2/c$, with lattice parameters $a = 9.3222(10)$ Å, $b = 9.5731(10)$ Å, $c = 13.3328(12)$ Å and $\beta = 90.101(5)°$. The crystal structure was solved by the intrinsic phasing method by SHELXT and refined with SHELXL against the F^2 data to the final R factor of 0.0246 (for 1,372 unique reflections with $F_O > 4$ s.d. (F_O)) with anisotropic displacement parameters for all non-hydrogen atoms, where F is structure factor, R is reliability factor and F_O is observed structure factor, and s.d. stands for standard deviation. Refinements of the occupancies of Mg and N sites were determined on the basis of the results of the elemental composition determination using EPMA. Ammonium ions were imposed by rigid-body geometry constraints, further releasing the N atom from a symmetry element allowed a flexible split of N inside a cage of six Cl^- vertices and decreased the anisotropic displacement parameters, giving a better fit to the collected X-ray intensities. The results of the crystallography data are presented in Supplementary Tables 2–5.

Cl isotope measurements in terrestrial samples using pulsed thermal ionization mass spectrometry (P-TIMS)

Growth of the terrestrial material as an isotopic standard. The chemicals NH_4Cl and $MgCl_2{\cdot}6H_2O$ were purchased from Sinopharm Reagent Corporation and were of analytical grade with a purity greater than 99.0%. They were used as received without any additional purification. Deionized water was used to prepare solutions and for subsequent chemical analysis. To prepare single crystals of $NH_4MgCl_3{\cdot}6H_2O$, a mixture of NH_4Cl and $MgCl_2{\cdot}6H_2O$ in a molar ratio of 1:1 was added to a beaker and stirred in distilled water until fully dissolved. The solution was then subjected to slow evaporation, resulting in the formation of colourless crystals of $NH_4MgCl_3{\cdot}6H_2O$ (ref. 53). The crystals obtained in this manner were used as the standard material for isotopic analysis and thermodynamic analysis.

Sample treatment of the terrestrial material for isotopic measurements. All samples were prepared using a two-step resin method. First, regenerated H-cation exchange resin (Dowex 50W × 8, 200–400 mesh) was packed into a polyethylene-accompanied ion-exchange column with a diameter of 0.4 cm and a resin height of 2 cm. Regenerated Cs-cation exchange resin was then packed into another polyethylene-accompanied ion-exchange column with a diameter of 0.4 cm and a resin height of 1.6 cm. The liquid samples were passed through the H-cation exchange resin column, in which all Cl in the samples transformed into HCl solution. The liquid then passed through the Cs-cation exchange resin column, and the CsCl solution collected was used for mass spectrometry analysis. The pH of the solution was neutral.

Procedure for the P-TIMS measurements. The Cl isotopes of the terrestrial material were analysed using P-TIMS in a Triton mass spectrometer[41]. The tantalum filament was heated with a current of 2.5 A for 1 h in a vacuum system and coated with 2.5 μl of graphite slurry (80% ethanol mixed with 80 μg of graphite) at the centre of the filament. The test solution, consisting of CsCl as the source of Cl, was loaded onto the filament and dried using a current of 1 A for 1.5 min. The samples were then placed in the mass spectrometer, and the measurement was initiated once the ion source was evacuated to a pressure lower than 2.5×10^{-7} mbar. The intensity of the Cs_2Cl^+ ion was adjusted to 4×10^{-12} A by controlling the filament current. Data were simultaneously collected on Faraday cup C and H1 by capturing the ion flow with mass numbers of 301 ($^{133}Cs_2{}^{35}Cl^+$) and 303 ($^{133}Cs_2{}^{37}Cl^+$).

The $\delta^{37}Cl$ values (in ‰) were calculated using the following equation:

$$\delta^{37}\mathrm{Cl} = \left[\left({}^{37}\mathrm{Cl}/{}^{35}\mathrm{Cl}\right)_{\mathrm{Sample}} / \left({}^{37}\mathrm{Cl}/{}^{35}\mathrm{Cl}\right)_{\mathrm{Standard}} - 1\right] \times 1000$$

The average value of the standard material ISL 354 NaCl was obtained from the results of three repeated determinations under the same conditions. The measured value of the international standard ISL 354 for chlorine isotopes was 0.319062 ± 0.00005. The measured $\delta^{37}Cl$ value of the terrestrial $NH_4MgCl_3{\cdot}6H_2O$ single crystals was 0.08‰ (relative to SMOC).

Measurement of Cl isotopes in ULM-1 using a nano secondary-ion mass spectrometer. The in situ Cl isotope measurements were performed in the NanoSIMS Lab at School of Earth system science, Tianjin University. The CAMECA NanoSIMS 50L secondary-ion mass spectrometer was used for Cl isotope measurements of ULM-1, the terrestrial $NH_4MgCl_3{\cdot}6H_2O$ crystals with a determined $\delta^{37}Cl$ (0.08‰ relative to SMOC) were used to calibrate the matrix effects and instrument mass fractionation of novograblenovite. To prepare the NanoSIMS specimen, flat pieces of terrestrial $NH_4MgCl_3{\cdot}6H_2O$ (160 × 120 × 15 μm^3) and ULM-1 (80 × 60 × 15 μm^3) crystals were fixed on a 10-mm-diameter Si disk with thin films of carbon paste. The spatial resolution of the analysis was ~100 nm using a Cs^+ primary beam with an intensity of 1 pA and an accelerating voltage of ~16 kV. Each analysis surface area with a raster size of 5 μm was divided into 64 × 64 pixels, with a counting time of 0.132 ms per pixel. The number of cycles was set at 300. Before analysis, 6 min of pre-sputtering using a 300 pA was performed on a larger area (30 × 30 μm^2) than the analysed surface to remove any contamination from the surface and establish sputter equilibrium. An electron flood gun was used for charge compensation. Secondary negative ions of ^{16}O, ^{35}Cl and ^{37}Cl were imaged by scanning ion imaging, with a mass resolving power of 6,000.

For Cl isotope measurements, the instrumental mass fractionation factor, α, based on analyses of the terrestrial crystal standard, was 1.0212 ± 0.0008 (2 s.d.). The measured $^{37}Cl/^{35}Cl$ ratios were corrected for instrument mass fractionation. The quasi-simultaneous arrival effect was calibrated using the relation[54,55]:

$$N_{\text{true}} = N_{\text{meas}} \times (1 + \zeta \times K)$$

where N_{meas} is the measured ion count, N_{true} is the true ion count, K is the average number of secondary ions ejected per primary ion, expressed as $I_{\text{secondary}}/I_{\text{primary}}$ (the intensity ratio of the secondary ions to the primary ions that hit the sample surface, that is, FCo), and ζ is the quasi-simultaneous arrival coefficient. The results of the Cl isotope data are presented in Supplementary Table 6.

Lunar and terrestrial materials. The lunar sample, designation CE5C0400YJFM00507 was provided by the China National Space Administration (CNSA) under a materials transfer agreement a half-year loan (with an extension for another half-year), after which they will be returned to CNSA. Readers may request Chang'e-5 samples from CNSA through a standard procedure. To obtain large enough samples (>1 mg) to measure the specific heat data of $(NH_4)MgCl_3{\cdot}6H_2O$ (S6) and $(NH_4)MgCl_3{\cdot}2H_2O$ (S2) for thermodynamic analysis, we synthesized high-purity crystals of S6 based on a modified solution method described above and in ref. 52. Powdered samples of S2 were obtained by heating S6 in air at 140 °C.

Thermodynamic analysis of the fugacity of water vapour. *S6*. The heat capacity of single crystals of S6 was measured in the Quantum Design physical property measurement system.

According to the Debye model, the heat capacity:

$$C_V(T) = 9NR(T/\theta_D)^3 \int_0^{\theta_D} \frac{x^4 e^x}{(e^x - 1)^2} dx$$

where V is the mole volume, T is the temperature, θ_D is the Debye temperature, R the ideal gas constant and $N = 27$ because there are 27 moles of atoms in each mole of S6.

According to the Einstein model, the heat capacity:

$$C_V(T) = 3NR\left(\frac{\theta_E}{T}\right)^2 \frac{e^{\frac{\theta_E}{T}}}{\left(e^{\frac{\theta_E}{T}} - 1\right)^2}$$

where θ_E is the Einstein temperature.

The Debye model can usually describe the heat capacity of a simple compound well. For crystals with weakly bonded structural units, such as S6 with $[Mg(H_2O)_6]$ and $[NH_4]$ blocks, additional Einstein models should be used to describe the local vibrations of such units. To fit the heat capacity of S6, one Debye model and two independent Einstein models were used.

By fitting the above equations to the measured data (Supplementary Tables 7 and 8) we obtained $C_V(T)$, as shown by the blue line in Supplementary Fig. 9.

Under constant pressure (P):

$$C_P(T) = C_V(T) + P\mathrm{d}V/\mathrm{d}T = C_V(T) + PV\left(\frac{\mathrm{d}V}{V\mathrm{d}T}\right)$$

Here V is the mole volume, $\mathrm{d}V/V\mathrm{d}T$ is thermal expansion coefficient.

At standard pressure, $P^o = 1.01 \times 10^5$ Pa, $V(S6) = 170.7 \times 10^{-6}$ m^3 mol^{-1}. For solid substances, $\mathrm{d}V/V\mathrm{d}T$ is typically smaller than 10^{-4}, so that $P\mathrm{d}V/V\mathrm{d}T$ is on the order of 10^{-3} J mol^{-1} K^{-1}, which can be safely ignored given that C_V is generally on the order of 10^5 J mol^{-1} K^{-1}. Here the fitted $C_V(T)$ is used as $C_P(T)$ for S6 without further correction.

The definitions of entropy and enthalpy are as follows:

$$S^o(T) = \int_0^T \frac{C_P(t)}{t} dt \quad (4)$$

$$H^o(T) = H^o(0) + \int_0^T C_P(t) dt \quad (5)$$

where t represents temperature. The entropy of the S6 crystal thus obtained is shown in Supplementary Fig. 10.

The formation of ULM-1 can be described by the following chemical equation during volcanic eruption:

$$6H_2O(g) + NH_3(g) + HCl(g) + MgCl_2(s) = (NH_4)MgCl_3{\cdot}6H_2O(s) \quad (6)$$

The entropy change in the formation of ULM-1 is then:

$$\Delta S^o = S^o\left((NH_4)MgCl_3{\cdot}6H_2O\right)^{\text{solid}} - 6 \times S^o(H_2O)^{\text{gas}} - S^o(NH_3)^{\text{gas}} - S^o(HCl)^{\text{gas}} - S^o(MgCl_2)^{\text{solid}}$$

The entropies of NH_3(g), HCl(g), H_2O(g) and $MgCl_2$(s) were taken from the National Institute of Standards and Technology Joint Army-Navy-Air Force (JANAF-NIST) thermodynamic database[56], and the resulting entropies are shown in Supplementary Fig. 11.

The enthalpy change in the formation of ULM-1 is then:

$$\Delta H^o = H^o\left((NH_4)MgCl_3{\cdot}6H_2O\right)^{\text{solid}} - 6 \times H^o(H_2O)^{\text{gas}} - H^o(NH_3)^{\text{gas}} - H^o(HCl)^{\text{gas}} - H^o(MgCl_2)^{\text{solid}}$$

Considering that ΔH^o is mostly contributed by the solid-to-gas transition, the equation can be rewritten as:

$$\begin{aligned}\Delta H^o = &\left\{H^o\left((NH_4)MgCl_3{\cdot}6H_2O\right)^{\text{solid}} - \left[6 \times H^o(H_2O)^{\text{solid}} + H^o(NH_4Cl)^{\text{solid}} + H^o(MgCl_2)^{\text{solid}}\right]\right\} \\ &+ \left\{\left[6 \times H^o(H_2O)^{\text{solid}} + H^o(NH_4Cl)^{\text{solid}} + H^o(MgCl_2)^{\text{solid}}\right] - \left[6 \times H^o(H_2O)^{\text{gas}} + H^o(NH_3)^{\text{gas}} + H^o(HCl)^{\text{gas}} + H^o(MgCl_2)^{\text{solid}}\right]\right\}\end{aligned}$$

Where we define the enthalpy change between a solid phase transition as:

$$\Delta H_1 = \left\{H^o\left((NH_4)MgCl_3{\cdot}6H_2O\right)^{\text{solid}} - \left[6 \times H^o(H_2O)^{\text{solid}} + H^o(NH_4Cl)^{\text{solid}} + H^o(MgCl_2)^{\text{solid}}\right]\right\}$$

And the enthalpy difference between solid and gaseous reagents is:

$$\begin{aligned}\Delta H_2 &= \left\{\left[6 \times H^o(H_2O)^{\text{solid}} + H^o(NH_4Cl)^{\text{solid}} + H^o(MgCl_2)^{\text{solid}}\right] - \left[6 \times H^o(H_2O)^{\text{gas}} + H^o(NH_3)^{\text{gas}} + H^o(HCl)^{\text{gas}} + H^o(MgCl_2)^{\text{solid}}\right]\right\} \\ &= \left\{6 \times \left[H^o(H_2O)^{\text{solid}} - H^o(H_2O)^{\text{gas}}\right] + \left[H^o(NH_4Cl)^{\text{solid}} - H^o(NH_3)^{\text{gas}} - H^o(HCl)^{\text{gas}}\right]\right\}\end{aligned}$$

At 0 K, ΔH_2 obtained from the JANAF-NIST thermodynamic database is:

$$\Delta H_2 = -463.179 \text{ kJ mol}^{-1}$$

Meanwhile, ΔH_1 is much smaller and its value at 0 K can be obtained using ab initio quantum chemistry calculations:

$$\Delta H_1 = -54.499\ \mathrm{kJ\ mol^{-1}}$$

So $\Delta H^{o}(0)$ in equation (5) is obtained as:

$$\Delta H^{o}(0) = \Delta H_1 + \Delta H_2 = -517.679\ \mathrm{kJ\ mol^{-1}}$$

At finite temperatures, the enthalpy change of equation (6) is determined by the specific heat difference between the product and the reagent:

$$\begin{aligned}\Delta H^{o}(\mathrm{T}) &= \Delta H^{o}(0) + \int_0^T \Delta C_P(t)\,\mathrm{d}t \\ &= \Delta H^{o}(0) + \int_0^T C_P^{((\mathrm{NH_4})\mathrm{MgCl_3}\cdot 6\mathrm{H_2O})^{\mathrm{solid}}}(t)\mathrm{d}t \\ &\quad - \int_0^T \left[6 \times C_P^{(\mathrm{H_2O})^{\mathrm{gas}}}(t) + C_P^{(\mathrm{HCl})^{\mathrm{gas}}}(t)\right. \\ &\quad \left. + C_P^{(\mathrm{NH_3})^{\mathrm{gas}}}(t) + C_P^{(\mathrm{MgCl_2})^{\mathrm{solid}}}(t)\right]\mathrm{d}t \\ &= \Delta H^{o}(0) + \int_0^T C_P^{((\mathrm{NH_4})\mathrm{MgCl_3}\cdot 6\mathrm{H_2O})^{\mathrm{solid}}}(t)\mathrm{d}t \\ &\quad - \left\{6 \times \left[H^{(\mathrm{H_2O})^{\mathrm{gas}}}(T) - H^{(\mathrm{H_2O})^{\mathrm{gas}}}(0)\right]\right. \\ &\quad + \left[H^{(\mathrm{HCl})^{\mathrm{gas}}}(T) - H^{(\mathrm{HCl})^{\mathrm{gas}}}(0)\right] \\ &\quad + \left[H^{(\mathrm{NH_3})^{\mathrm{gas}}}(T) - H^{(\mathrm{NH_3})^{\mathrm{gas}}}(0)\right] \\ &\quad \left. + \left[H^{(\mathrm{MgCl_2})^{\mathrm{solid}}}(T) - H^{(\mathrm{MgCl_2})^{\mathrm{solid}}}(0)\right]\right\}\end{aligned}$$

Based on the ΔH data taken from the JANAF-NIST thermodynamic database and the fitted specific heat of ULM-1, $\Delta H^{o}(T)$ is shown in Supplementary Fig. 12.

The reaction Gibbs free energy of chemical equation (6) can be obtained from the reaction entropy and reaction enthalpy:

$$\Delta G^{o} = \Delta H^{o} - T\Delta S^{o},$$

which is shown in Supplementary Fig. 13.

According to the chemical reaction isotherm:

$$\ln K = -\Delta G_{\mathrm{r}}^{o}(T)/RT$$

where K is the equilibrium constant and the subscript r denotes chemical reaction; the result is shown in Supplementary Fig. 14.

Therefore, the equilibrium constant for reaction (equation (6)) of the hexahydrate (K_6) can be obtained by:

$$\log K_6 = \frac{-\Delta G_{\mathrm{r}}^{o}(T)}{\ln 10 \times RT}$$

Then K_6 of reaction (equation (6)) is:

$$K_6 = \frac{1}{\left[\frac{f_{\mathrm{H_2O}}}{P^{o}}\right]^6 \frac{f_{\mathrm{HCl}}}{P^{o}} \frac{f_{\mathrm{NH_3}}}{P^{o}}}.$$

Therefore:

$$\log K_6 = \frac{-\Delta G_6^{o}(T)}{\ln 10 \times RT} = -\left\{6\log\left[\frac{f_{(\mathrm{H_2O})}}{P^{o}}\right] + \log\frac{f_{\mathrm{HCl}}}{P^{o}} + \log\frac{f_{\mathrm{NH_3}}}{P^{o}}\right\} \quad (7)$$

The sum of f_{HCl} and $f_{\mathrm{NH_3}}$ in volcanic gases is thermodynamically constrained by a well-known chemical reaction:

$$\mathrm{NH_2(g) + HCl(g) = NH_4Cl(s)} \quad (8)$$

Similarly, we have:

$$\log K_{\mathrm{NH_4Cl}} = \frac{-\Delta G_{\mathrm{NH_4Cl}}^{o}(T)}{\ln 10 \times RT} = -\left\{\log\frac{f_{\mathrm{HCl}}}{P^{o}} + \log\frac{f_{\mathrm{NH_3}}}{P^{o}}\right\},$$

which sets a thermodynamic maximum value of $\left\{\log\frac{f_{\mathrm{HCl}}}{P^{o}} + \log\frac{f_{\mathrm{NH_3}}}{P^{o}}\right\}$

$$\left\{\log\frac{f_{\mathrm{HCl}}}{P^{o}} + \log\frac{f_{\mathrm{NH_3}}}{P^{o}}\right\}^{\max} = \frac{\Delta G_{\mathrm{NH_4Cl}}^{o}(T)}{\ln 10 \times RT}, \quad (9)$$

which is shown in Supplementary Fig. 15.

Combining equations (7) and (9), we have:

$$\begin{aligned}6\log\left[\frac{f_{\mathrm{H_2O}}}{P^{o}}\right] &= \frac{\Delta G_6^{o}(T)}{\ln 10 \times RT} - \left\{\log\frac{f_{\mathrm{HCl}}}{P^{o}} + \log\frac{f_{\mathrm{NH_3}}}{P^{o}}\right\} > \frac{\Delta G_6^{o}(T)}{\ln 10 \times RT} \\ &\quad - \left\{\log\frac{f_{\mathrm{HCl}}}{P^{o}} + \log\frac{f_{\mathrm{NH_3}}}{P^{o}}\right\}^{\max} = \frac{\Delta G_6^{o}(T) - \Delta G_{\mathrm{NH_4Cl}}^{o}(T)}{\ln 10 \times RT}\end{aligned}$$

so we can obtain the thermodynamic lower limit of $f_{\mathrm{H_2O}}$:

$$\left\{\log\left[\frac{f_{\mathrm{H_2O}}}{P^{o}}\right]\right\}^{\min} = \frac{\Delta G_6^{o}(T) - \Delta G_{\mathrm{NH_4Cl}}^{o}(T)}{\ln 10 \times 6RT}. \quad (10)$$

$\Delta G_6^{o}(T)$ is shown in Supplementary Fig. 13, and $\Delta G_{\mathrm{NH_4Cl}}^{o}(T)$ was obtained from the JANAF-NIST thermodynamic database based on the formation Gibbs energy of NH_4Cl(s), NH_3(g) and HCl(g). The resulting $\left\{\log\left[\frac{f_{\mathrm{H_2O}}}{P^{o}}\right]\right\}^{\min}$ for S6 is shown in Fig. 4.

S2. Similarly to the thermodynamic analysis shown above for S6, the heat capacity, reaction entropy, reaction enthalpy, reaction Gibbs free energy, equilibrium constant and minimum fugacity of water can also be obtained for S2 following equation (11):

$$\mathrm{2H_2O(g) + NH_3(g) + HCl(g) + MgCl_2(s) = (NH_4)MgCl_3\cdot 2H_2O(s)} \quad (11)$$

The heat capacity of the powdered S2 sample was measured in the Quantum Design physical property measurement system. By fitting the Debye and Einstein equations to the measured data (Supplementary Tables 7 and 9), the function $C_V(T)$ was obtained, as shown by the blue line in Supplementary Fig. 16.

The entropy change in the formation of S2 is then:

$$\begin{aligned}\Delta S^{o} &= S^{o}\left((\mathrm{NH_4})\,\mathrm{MgCl_3}\cdot 2\mathrm{H_2O}\right)^{\mathrm{solid}} - 2 \times S^{o}(\mathrm{H_2O})^{\mathrm{gas}} - S^{o}(\mathrm{NH_3})^{\mathrm{gas}} \\ &\quad - S^{o}(\mathrm{HCl})^{\mathrm{gas}} - S^{o}(\mathrm{MgCl_2})^{\mathrm{solid}}\end{aligned}$$

the result of which is shown in Supplementary Fig. 17.

The entropy of NH_3(g), HCl(g), H_2O(g) and $MgCl_2$(s) were taken from the JANAF-NIST thermodynamic database, and the resulting entropies are shown in Supplementary Fig. 18.

The enthalpy change in the formation of S2 is:

$$\begin{aligned}\Delta H_2 &= H^{o}\left((\mathrm{NH_4})\,\mathrm{MgCl_3}\cdot 2\mathrm{H_2O}\right)^{\mathrm{solid}} - 2 \times H^{o}(\mathrm{H_2O})^{\mathrm{gas}} - H^{o}(\mathrm{NH_3})^{\mathrm{gas}} \\ &\quad - H^{o}(\mathrm{HCl})^{\mathrm{gas}} - H^{o}(\mathrm{MgCl_2})^{\mathrm{solid}}\end{aligned}$$

Given that ΔH during the decomposition of S6 to S2 is known, ΔH_2 can be obtained based on ΔH_6 and the heat capacities of S6, S2 and H_2O vapours:

$$\begin{aligned}&\Delta H_6 - \Delta H_2 \\ &= H^{o}\left((\mathrm{NH_4})\,\mathrm{MgCl_3}\cdot 6\mathrm{H_2O}\right)^{\mathrm{solid}} - H^{o}\left((\mathrm{NH_4})\,\mathrm{MgCl_3}\cdot 2\mathrm{H_2O}\right)^{\mathrm{solid}} \\ &\quad - 4 \times H^{o}(\mathrm{H_2O})^{\mathrm{gas}}\end{aligned}$$

The right side of the above equation is the enthalpy change during the decomposition of S6 to S2 and water vapour, which is defined by:

$$\Delta H^{D}(T) = \Delta H^{D}(T^{D}) + \int_{T^{D}}^{T} \Delta C_{P}(t)\,\mathrm{d}t = \Delta H^{D}(T^{D}) + \int_{T^{D}}^{T} C_{P}^{((NH_4)MgCl_3\cdot 6H_2O)^{solid}}(t) - C_{P}^{((NH_4)MgCl_3\cdot 2H_2O)^{solid}}(t) - 4C_{P}^{(H_2O)^{gas}}(t)\,\mathrm{d}t$$

where superscript D is used to denote decomposition; we have:

$$\Delta H_2(t) = \Delta H_6(t) - \left\{\Delta H^{D}(T^{D}) + \int_{T^{D}}^{T} C_{P}^{((NH_4)MgCl_3\cdot 6H_2O)^{solid}}(t) - C_{P}^{((NH_4)MgCl_3\cdot 2H_2O)^{solid}}(t) - 4C_{P}^{(H_2O)^{gas}}(t)\,\mathrm{d}t\right\}$$

where $\Delta H^{D}(T_D)$ is reported to be 240 ± 20 kJ mol^{-1}, T_D is reported to be 428 K (ref. 57), $\Delta H_6(t)$ was taken from Supplementary Fig. 12, and the heat capacities of S6, S2 and water (gas) were taken from Supplementary Figs. 9 and 16 and the JANAF-NIST thermodynamic database.

$\Delta H_2(t)$ can thus be obtained and is shown in Supplementary Fig. 19.

The reaction Gibbs free energy of chemical equation (11) can be obtained from the reaction entropy and reaction enthalpy:

$$\Delta G^{o} = \Delta H^{o} - T\Delta S^{o},$$

the result of which is shown in Supplementary Fig. 20.

K and f_{H_2O} for S2 can then be obtained by a similar thermodynamic analysis to S6:

$$\ln K = -\Delta G_{r}^{o}(T)/RT$$

Therefore, the equilibrium constant for reaction equation (11) of S2 (K_2) can be obtained as:

$$\log K_2 = \frac{-\Delta G_{r}^{o}(T)}{\ln 10 \times RT},$$

which is shown in Supplementary Fig. 21.

K_2 of reaction equation (6) is:

$$K_2 = \frac{1}{\left[\frac{f_{H_2O}}{P^{o}}\right]^{2}\frac{f_{HCl}}{P^{o}}\frac{f_{NH_3}}{P^{o}}},$$

therefore:

$$\log K_2 = \frac{-\Delta G_{2}^{o}(T)}{\ln 10 \times RT} = -\left\{2\log\left[\frac{f_{H_2O}}{P^{o}}\right] + \log\frac{f_{HCl}}{P^{o}} + \log\frac{f_{NH_3}}{P^{o}}\right\}. \quad (12)$$

Incorporating the thermodynamic maximum value of $\left\{\log\frac{f_{HCl)}}{P^{o}} + \log\frac{f_{NH_3}}{P^{o}}\right\}$ based on equation (9) with equation (12), we have:

$$2\log\left[\frac{f_{H_2O}}{P^{o}}\right] = \frac{\Delta G_{2}^{o}(T)}{\ln 10 \times RT} - \left\{\log\frac{f_{HCl}}{P^{o}} + \log\frac{f_{NH_3}}{P^{o}}\right\} > \frac{\Delta G_{2}^{o}(T)}{\ln 10 \times RT} - \left\{\log\frac{f_{HCl}}{P^{o}} + \log\frac{f_{NH_3}}{P^{o}}\right\}^{max} = \frac{\Delta G_{2}^{o}(T) - \Delta G_{NH_4Cl}^{o}(T)}{\ln 10 \times RT},$$

so we can obtain the thermodynamic lower limit of f_{H_2O}:

$$\left\{\log\left[\frac{f_{H_2O}}{P^{o}}\right]\right\}^{min} = \frac{\Delta G_{2}^{o}(T) - \Delta G_{NH_4Cl}^{o}(T)}{\ln 10 \times 2RT}. \quad (13)$$

$\Delta G_{2}^{o}(T)$ is shown in Supplementary Fig. 20, $\Delta G_{NH_4Cl}^{o}(T)$ was obtained from the JANAF-NIST thermodynamic database and the resulting $\left\{\log\left[\frac{f_{H_2O}}{P^{o}}\right]\right\}^{min}$ for S2 is shown in Fig. 4.

H_2 and H_2O gases in magma. The stability of water in lunar magma is governed by the reaction:

$$H_2O = H_2 + 1/2O_2 \quad (14)$$

and is therefore a function of both the oxygen and hydrogen fugacities of the system. Thermodynamically, reaction (equation (14)) is governed by the equation:

$$\ln\frac{\left[\frac{f_{H_2O}}{P^{o}}\right]}{\frac{f_{H_2}}{P^{o}}\left[\frac{f_{O_2}}{P^{o}}\right]^{1/2}} = -\Delta G_{r}^{o}(T)/RT;$$

there are no reliable mineral buffers for the hydrogen fugacity of lunar materials, but the f_{O_2} of the Moon can be used to estimate f_{H_2}/f_{H_2O} ratios.

The f_{O_2} of the lunar mineral assemblages and lunar igneous rocks has been intensively investigated and is found clustered around the Fe–ilmenite–ulvöspinel buffer:

$$2Fe + 2FeTiO_3 + O_2 = 2Fe_2TiO_4,$$

which is shown in Supplementary Fig. 22.

The melting and crystallization relationships in synthetic melts of mare basalt composition have been extensively studied in the laboratory. The temperature at which the molten high-Ti mare basalts begin to crystallize, called the liquidus temperature, is generally around 1,150 °C (ref. 18). When the basalts are heated, they start to melt at around 1,050 °C—this melting temperature is about 100 °C higher than those of terrestrial basalts, chiefly because of the lake of H_2O in returned lunar basalts[18]. Based on the $\Delta G_{r}^{o}(T)$ values obtained from the JANAF-NIST thermodynamic database, the calculated f_{H_2}/f_{H_2O} ratio at the Fe–ilmenite–ulvöspinel buffer and 1,100 °C magma temperature is 2.95. In other words, H_2 is the predominant vapour species in the O–H system at the low f_{O_2} of the Moon. It is worth noting that Newcombe et al.[19] also examined the solubility of H_2 and H_2O in lunar magmas, estimating a very similar f_{H_2}/f_{H_2O} ratio of around 2.67 (19). The results of Newcombe et al. and our thermodynamic calculations were both used to estimate f_{H_2}/f_{H_2O} values. The resulting $\left\{\log\left[\frac{f_{H_2O}+f_{H_2}}{P^{o}}\right]\right\}^{min}$ values constrained by the formation of S6 are shown in Fig. 4.

Data availability

All data are available in the main text or the Supplementary Information. The X-ray crystallographic coordinates of the structures reported in this study have been deposited at the Cambridge Crystallographic Data Centre (CCDC) under deposition number 2166870. These data can be obtained free of charge from the Cambridge Crystallographic Data Centre via www.ccdc.cam.ac.uk/data_request/cif. Source data are provided with this paper.

References

1. Canup, R. M. & Asphaug, E. Origin of the Moon in a giant impact near the end of the Earth's formation. *Nature* **412**, 708–712 (2001).
2. Asimow, P. D. & Langmuir, C. H. The importance of water to oceanic mantle melting regimes. *Nature* **421**, 815–820 (2003).
3. Sigurdsson, H. (ed.) *Encyclopedia of Volcanoes* 1st edn (Academic, 1999).
4. Lunar Science Preliminary Examination Team. Preliminary examination of lunar samples from Apollo 12. *Science* **167**, 1325–1339 (1970).
5. Albarède, F. Volatile accretion history of the terrestrial planets and dynamic implications. *Nature* **461**, 1227–1233 (2009).

6. Warren, P. H. The magma ocean concept and lunar evolution. *Annu. Rev. Earth Planet. Sci.* **13**, 201–240 (1985).
7. Shearer, C. K. et al. Thermal and magmatic evolution of the moon. *Rev. Mineral. Geochem.* **60**, 365–518 (2006).
8. Anand, M. Lunar water: a brief review. *Earth Moon Planets* **107**, 65–73 (2010).
9. Saal, A. E. et al. Volatile content of lunar volcanic glasses and the presence of water in the Moon's interior. *Nature* **454**, 192–195 (2008).
10. Hauri, E. H., Weinreich, T., Saal, A. E., Rutherford, M. C. & Orman, J. A. High pre-eruptive water contents preserved in lunar melt inclusions. *Science* **333**, 213–215 (2011).
11. Boyce, J. W. et al. Lunar apatite with terrestrial volatile abundances. *Nature* **466**, 466–469 (2010).
12. Hui, H. J., Peslier, A. H., Zhang, Y. X. & Neal, C. R. Water in lunar anorthosites and evidence for a wet early Moon. *Nat. Geosci.* **6**, 177–180 (2013).
13. Sharp, Z. D., Shearer, C. K., McKeegan, K. D., Barnes, J. D. & Wang, Y. Q. The chlorine isotope composition of the Moon and implications for an anhydrous mantle. *Science* **329**, 1050–1053 (2010).
14. McCubbin, F. M. et al. Magmatic volatiles (H, C, N, F, S, Cl) in the lunar mantle, crust, and regolith: abundances, distributions, processes, and reservoirs. *Am. Mineral.* **100**, 1668–1707 (2015).
15. Pieters, C. M. et al. Character and spatial distribution of OH/H_2O on the surface of the moon seen by M^3 on Chandrayaan-1. *Science* **326**, 568–572 (2009).
16. Colaprete, A. et al. Detection of water in the LCROSS ejecta plume. *Science* **330**, 463–468 (2010).
17. Slade, M. A., Butler, B. J. & Muhleman, D. O. Mercury radar imaging: evidence for polar ice. *Science* **258**, 635–640 (1992).
18. Heiken, G. H., Vaniman, D. T. & French, B. M. *The Lunar Source Book* (Cambridge Univ. Press, 1991).
19. Newcombe, M. E. et al. Solubility of water in lunar basalt at low pH_2O. *Geochim. Cosmochim. Acta* **200**, 330–352 (2017).
20. Kerr, R. A. How wet the Moon? Just damp enough to be interesting. *Science* **330**, 434 (2010).
21. Honniball, C. I. et al. Molecular water detected on the sunlit Moon by SOFIA. *Nat. Astron.* **5**, 121–127 (2021).
22. Qian, Y. Q., Xiao, L. & Zhao, S. Y. Geology and scientific significance of the Rümker region in northern Oceanus Procellarum: China's Chang'E-5 landing region. *J. Geophys. Res.* **123**, 1407–1430 (2018).
23. Che, X. et al. Age and composition of young basalts on the Moon, measured from samples returned by Chang'e-5. *Science* **374**, 887–890 (2021).
24. Li, Q. L. et al. Two-billion-year-old volcanism on the Moon from Chang'e-5 basalts. *Nature* **600**, 54–58 (2021).
25. Lin, H. et al. In situ detection of water on the Moon by the Chang'E-5 lander. *Sci. Adv.* **8**, eabl9174 (2022).
26. Hu, S. et al. A dry lunar mantle reservoir for young mare basalts of Chang'e-5. *Nature* **600**, 49–53 (2021).
27. Liu, J. J. et al. Evidence of water on the lunar surface from Chang'E-5 in-situ spectra and returned samples. *Nat. Commun.* **13**, 3119 (2022).
28. Guo, J. G. et al. Surface microstructures of lunar soil returned by Chang'e-5 mission reveal an intermediate stage in space weathering process. *Sci. Bull.* **67**, 1696–1701 (2022).
29. Haas, C. & Hornig, D. Inter-and intramolecular potentials and the spectrum of ice. *J. Chem. Phys.* **32**, 1763–1769 (1960).
30. Nakamoto, K. *Infrared and Raman Spectra of Inorganic and Coordination Compounds* (John Wiley & Sons, 2008).
31. Okrugin, V. M. et al. The new mineral novograblenovite, (NH_4,K)$MgCl_3$·$6H_2O$ from the Tolbachik volcano, Kamchatka, Russia: mineral description and crystal structure. *Mineral. Mag.* **83**, 223–231 (2019).
32. Parafiniuk, J., Stachowicz, M. & Woźniak, K. Novograblenovite from Radlin, Upper Silesia, Poland and its relation to 'redikortsevite'. *Mineral. Mag.* **85**, 132–141 (2021).
33. Schlemper, E. O., Sen Gupta, P. K. & Zoltai, T. Refinement of the structure of carnallite, $Mg(H_2O)_6KCl_3$. *Am. Mineral.* **70**, 1309–1313 (1985).
34. Barnes, J. D. & Sharp, Z. D. Chlorine isotope geochemistry. *Rev. Mineral. Geochem.* **82**, 345–378 (2017).
35. Boyce, J. W. The chlorine isotope fingerprint of the lunar magma ocean. *Sci. Adv.* **1**, e1500380 (2015).
36. Wang, Y., Hsu, W. & Guan, Y. An extremely heavy chlorine reservoir in the Moon: insights from the apatite in lunar meteorites. *Sci. Rep.* **9**, 5727 (2019).
37. Lin, Y. H. & Westrenen, W. V. Isotopic evidence for volatile replenishment of the Moon during the Late Accretion. *Natl Sci. Rev.* **6**, 1247–1254 (2019).
38. Sarafian, A. R., John, T., Roszjar, J. & Whitehouse, M. J. Chlorine and hydrogen degassing in Vesta's magma ocean. *Earth Planet. Sci. Lett.* **459**, 311–319 (2017).
39. Dhooghe, F., Keyser, J. D. & Hänni, N. Chlorine-bearing species and the $^{37}Cl/^{35}Cl$ isotope ratio in the coma of comet 67P/Churyumov–Gerasimenko. *Mon. Not. R. Astron. Soc.* **508**, 1020–1032 (2021).
40. Williams, J. T. et al. The chlorine isotopic composition of Martian meteorites 1: chlorine isotope composition of Martian mantle and crustal reservoirs and their interactions. *Meteorit. Planet. Sci.* **51**, 2092–2110 (2016).
41. Gui, J. Y., Chen, X., Han, X. D., Wang, Z. & Ma, Y. Q. Determination of stable chlorine isotopes by isotopic preparative chromatography (IPC) with positive–thermal ionization mass spectrometry (P-TIMS). *Anal. Lett.* **55**, 2564–2573 (2022).
42. Taylor, L. A., Mao, H. K. & Bell, P. M. Identification of the hydrated iron oxide mineral Akaganéite in Apollo 16 lunar rocks. *Geology* **2**, 429–432 (1974).
43. Williams, J. P., Paige, D. A., Greenhagen, B. T. & Sefton-Nash, E. The global surface temperatures of the Moon as measured by the Diviner Lunar Radiometer Experiment. *Icarus* **283**, 300–325 (2017).
44. Xiao, X. et al. Thermophysical properties of the regolith on the lunar far side revealed by the in situ temperature probing of the Chang'E-4 mission. *Natl Sci. Rev.* **9**, nwac175 (2022).
45. Zolotarev, A. A. et al. Crystal chemistry and high-temperature behaviour of ammonium phases NH_4MgCl_3·$6H_2O$ and $(NH_4)_2Fe^{3+}Cl_5$·H_2O from the burned dumps of the chelyabinsk coal basin. *Minerals* **9**, 486 (2019).
46. Milliken, R. E. & Li, S. Remote detection of widespread indigenous water in lunar pyroclastic deposits. *Nat. Geosci.* **10**, 561–656 (2017).
47. Koepenick, K. W. et al. Volatile emissions from the crater and flank of Oldoinyo Lengai volcano, Tanzania. *J. Geophys. Res.* **101**, 13819–13830 (1996).
48. Sharp, Z. D., McCubbin, F. M. & Shearer, C. K. A hydrogen-based oxidation mechanism relevant to planetary formation. *Earth Planet. Sci. Lett.* **380**, 88–97 (2013).
49. Gladstone, G. R. et al. LRO-LAMP observations of the LCROSS impact plume. *Science* **330**, 472–476 (2010).
50. Brown, J. D. in *Microbeam Analysis* (ed. Newbury, D. E.) 271–272 (San Francisco Press, 1988).
51. Van Borm, W. A. & Adams, F. C. A standardless ZAF correction for semi-quantitative electron probe microanalysis of microscopical particles. *X-Ray Spectrometry* **20**, 51–62 (1991).
52. Sheldrick, G. M. A short history of SHELX. *Acta Crystallogr. A* **64**, 112–122 (2008).
53. Solans, X., Font-Altaba, M., Aguilo, M., Solans, J. & Domenech, V. Crystal form and structure of ammonium hexaaquamagnesium trichloride, $NH_4(Mg(H_2O)_6)Cl_3$. *Acta Crystallogr. C* **39**, 1488–1490 (1983).

54. Slodzian, G., Hillion, F., Stadermann, F. J. & Zinner, E. QSA influences on isotopic ratio measurements. *Appl. Surf. Sci.* **231**, 874–877 (2004).
55. Slodzian, G., Chaintreau, M., Dennebouy, R. & Rousse, A. Precise in situ measurements of isotopic abundances with pulse counting of sputtered ions. *Eur. Phys. J.-Appl. Phys.* **14**, 199–231 (2001).
56. Chase, M. W. Jr *NIST-JANAF Thermochemical Tables* (National Institute of Standards and Technology, 1998).
57. Ball, M. C. & Ladner, N. G. Dehydration of ammonium magnesium chloride hexahydrate (ammonium carnallite). *J. Chem. Soc. Dalton Trans*. https://doi.org/10.1039/DT9790000330 (1979).

Acknowledgements

The CE5 lunar sample CE5C0400YJFM00507 (1.5 g) was provided by the China National Space Administration. We thank Y. Li, Q. Zhang, X. Wang, K. Ma, Q. Li, J. Zhou and T. Ying from the IOP, CAS, C. Sun from Tianjin University and C. Li and B. Liu from the National Astronomical Observatories, CAS, for their assistance in experiments and useful discussions. This work was supported by the Key Research Program of Chinese Academy of Sciences (grant number ZDBS-SSW-JSC007-2 to Xiaolong Chen), the Strategic Priority Research Program and Key Research Program of Frontier Sciences of the Chinese Academy of Sciences (grant number XDB33010100 to Xiaolong Chen), the Informatization Plan of Chinese Academy of Sciences (grant number CAS-WX2021SF-0102 to S.J.), the National Natural Science Foundation of China (grant number 52272268 to S.J.) and the Youth Innovation Promotion Association of CAS (grant number 2019005 to S.J.). This work was also supported by the Synergetic Extreme Condition User Facility (SECUF).

Author contributions

S.J. conducted the sample selection, EDS, EPMA, IR, Raman and isotopic experiments, thermodynamic calculations and data analysis and wrote the manuscript. M.H. conducted the sample selection, singled out the ULM-1 crystal and determined the crystal structure. Z.G. performed thermodynamic calculations. B.Y. performed isotopic experiments. Yuxin Ma performed EDS experiments. L.D. performed EPMA measurements. Xu Chen captured the optical photographs. Y.S., C. Cao and C. Chai performed Raman experiments. Q.W. and Yunqi Ma performed isotopic experiments. J.G. performed Raman experiments. Xialong Chen supervised the project, analysed the data and wrote the manuscript.

Competing interests

The authors declare no competing interests.

Additional information

Supplementary information The online version contains supplementary material available at https://doi.org/10.1038/s41550-024-02306-8.

Correspondence and requests for materials should be addressed to Xiaolong Chen.

Peer review information *Nature Astronomy* thanks Sabrina Schwinger and the other, anonymous, reviewer(s) for their contribution to the peer review of this work.